

## DIRECT OBSERVATIONS OF THE MAGNETIC RECONNECTION SITE OF AN ERUPTION ON 2003 NOVEMBER 18

J. LIN,<sup>1</sup> Y.-K. KO,<sup>1</sup> L. SUI,<sup>2</sup> J. C. RAYMOND,<sup>1</sup> G. A. STENBORG,<sup>2</sup> Y. JIANG,<sup>3</sup> S. ZHAO,<sup>3</sup> AND S. MANCUSO<sup>1,4</sup>

Received 2004 August 16; accepted 2004 December 3

### ABSTRACT

We report direct observations of the magnetic reconnection site during an eruptive process that occurred on 2003 November 18. The event started with a rapid expansion of a few magnetic arcades located over the east limb of the Sun and developed an energetic partial-halo coronal mass ejection (CME), a long current sheet, and a group of bright flare loops in the wake of the CME. It was observed by several instruments, both in space and on the ground, including the EUV Imaging Telescope, Ultraviolet Coronagraph Spectrometer, and Large Angle Spectrometric Coronagraph experiment on board the *Solar and Heliospheric Observatory*, the *Reuven Ramaty High Energy Solar Spectroscopic Imager*, and the Mauna Loa Solar Observatory Mark IV K-Coronameter. We combine the data from these instruments to investigate various properties of the eruptive process, including those around the current sheet. The maximum velocities of the CME leading edge and the core were 1939 and 1484 km s<sup>-1</sup>, respectively. The average reconnection inflow velocities near the current sheet over different time intervals ranged from 10.5 to 106 km s<sup>-1</sup>, and the average outflow velocities ranged from 460 to 1075 km s<sup>-1</sup>. This leads to a corresponding rate of reconnection in terms of the Alfvén Mach number  $M_A$  ranging from 0.01 to 0.23. The composite of images from different instruments specifies explicitly how the different objects developed by a single eruptive process are related to one another.

*Subject headings:* Sun: coronal mass ejections (CMEs) — Sun: flares — Sun: magnetic fields

*Online material:* mpeg animations

### 1. INTRODUCTION

The catastrophe model of solar eruptions suggests that the major eruptive processes occurring in the solar atmosphere are triggered by the catastrophic loss of mechanical equilibrium in the magnetic configuration (e.g., Forbes 2000; Priest & Forbes 2002; Lin et al. 2003). As the catastrophe takes place, the closed magnetic field lines in the configuration are stretched so severely that they effectively open up, and a current sheet forms separating two magnetic fields of opposite polarity. With dissipation occurring in the current sheet, the stretched field lines reconnect and create new closed field lines below the current sheet (see Fig. 1). Generally, the timescale of magnetic dissipation or reconnection is long compared with that of the catastrophe, which is the Alfvén timescale, so the development of a long current sheet is expected during major eruptions (Lin & Forbes 2000; Forbes & Lin 2000; Lin 2002).

As indicated by Figure 1, the current sheet is dissipated by magnetic reconnection, so that the catastrophe is able to develop into a plausible eruption. Subsequently, reconnection dumps a large amount of energy into the lower atmosphere of the Sun, which accounts for the traditional flare ribbons and loops; meanwhile, magnetic reconnection also sends large amounts of the reconnected flux and plasma upward, accounting for the rapid expansion of the ejecta and the hot shell surrounding it (see, e.g., Lin et al. 2004).

As a result of the high electrical conductivity and the force-free environment in the corona, the current sheet is confined to a very local and thin region. This makes direct observations of the current sheet extremely difficult (see Ko et al. 2003 for a discussion and brief review of this issue). Therefore, information about magnetic reconnection inside the current sheet is usually deduced indirectly by observing the dynamic behavior of the products of magnetic reconnection: the separating flare ribbons on the solar surface (Poletto & Kopp 1986; Qiu et al. 2002; Wang et al. 2003; Qiu et al. 2004), the growing flare loops in the corona (Sui & Holman 2003; Sui et al. 2004), and so on. A magnetic reconnection inflow around an X-type neutral point over flare loops has also been reported and used to analyze the properties of magnetic reconnection in an eruptive process (Yokoyama et al. 2001).

Using ultraviolet spectroscopic observations from the Ultraviolet Coronagraph Spectrometer (UVCS) on board the *Solar and Heliospheric Observatory (SOHO)* together with other remote-sensing data, Ciaravella et al. (2002) and Ko et al. (2003) have conducted comprehensive analyses of various aspects of several eruptive processes that clearly manifested both coronal mass ejections (CMEs) and solar flares, and they confirmed the existence and development of a long current sheet in the events as predicted by Lin & Forbes (2000) and Lin (2002). Webb et al. (2003) surveyed 59 CMEs observed by the *Solar Maximum Mission* from 1984 to 1989 and found that about half were followed by coaxial, bright rays suggestive of newly formed current sheets. They concluded that the characteristics of these structures were consistent with the Lin-Forbes model.

The event of 2003 November 18 provides us with another opportunity to directly observe the presumed current sheet and the associated magnetic reconnection process. It was observed by instruments both in space and on the ground. We present the observational data and give the corresponding results in the

<sup>1</sup> Harvard-Smithsonian Center for Astrophysics, 60 Garden Street, Cambridge, MA 02138.

<sup>2</sup> Department of Physics, Catholic University of America, 620 Michigan Avenue, Washington, DC 20064.

<sup>3</sup> Yunnan Observatory, National Astronomical Observatories, Chinese Academy of Sciences, P.O. Box 110, 650011 Kunming, China.

<sup>4</sup> Osservatorio Astronomico di Torino, INAF, 20 Strada Osservatorio, I-10025 Pino Torinese, Italy.

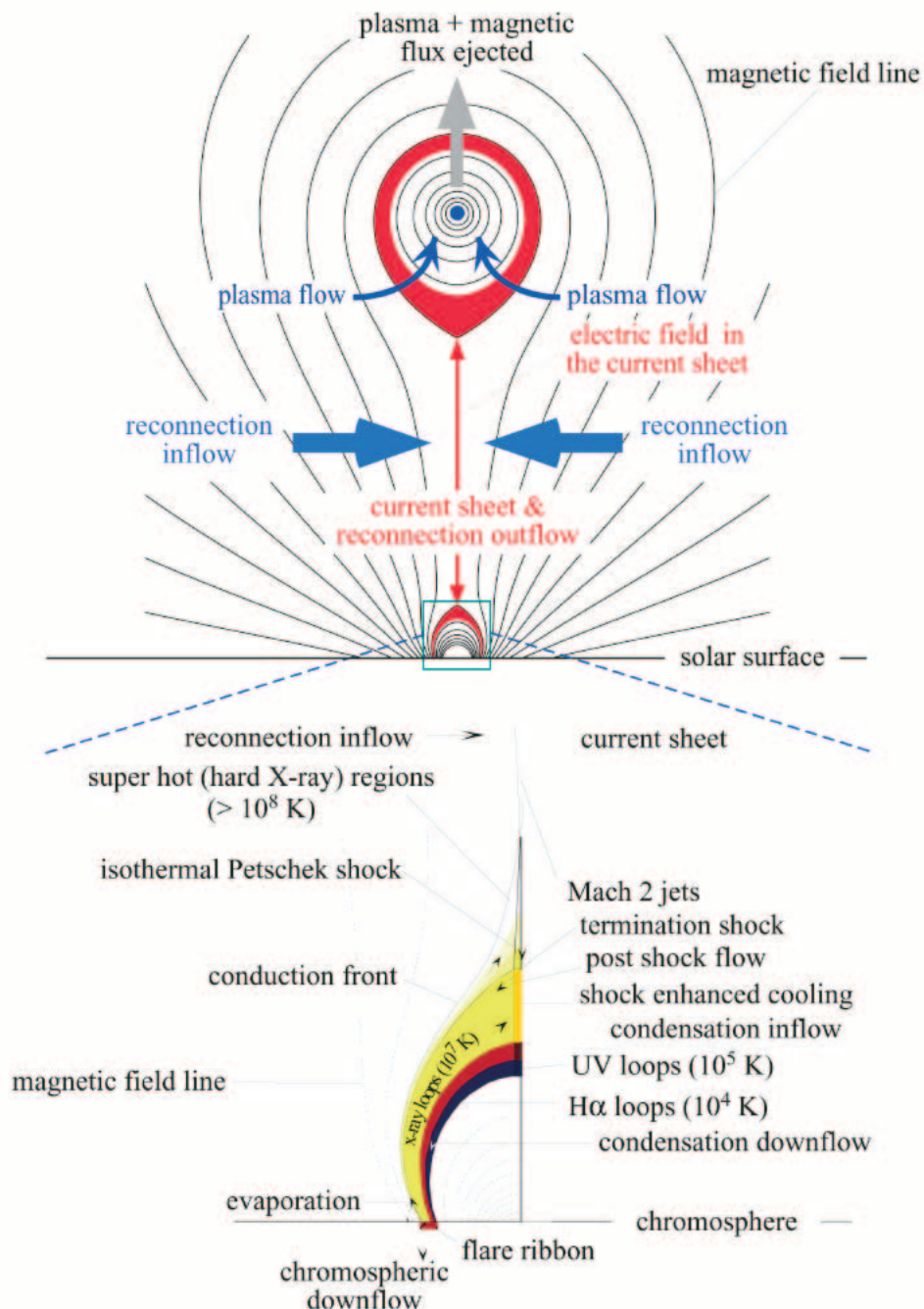


FIG. 1.—Schematic diagram of a disrupted magnetic field forming in an eruptive process. Colors are used to roughly denote the plasma layers at different temperatures. This diagram incorporates the two-ribbon flare configuration of Forbes & Acton (1996) and the CME configuration of Lin & Forbes (2000). More discussion about the CME part can be found in Lin et al. (2004).

next section and then discuss and summarize the present work in § 3.

## 2. OBSERVATIONS AND RESULTS

This event occurred on the east limb of the Sun. No apparent magnetic structure appeared in the nearby region in  $H\alpha$  filtergrams. After having looked at both the magnetograms obtained by the Michelson Doppler Imager (MDI) on board *SOHO* and the  $H\alpha$  images obtained on the ground within the following 3 days, we find that the eruption took place between NOAA Active Regions 0507 and 0508, located north and south of it, respectively, but its relation to these two active regions is not clear. On the other hand, the initial stage and subsequent develop-

ment of the eruption in the lower corona were clearly recorded at  $195 \text{ \AA}$  by the EUV Imaging Telescope (EIT) on *SOHO* and by the *Reuven Ramaty High Energy Solar Spectroscopic Imager (RHESSI)*; Lin et al. 2002). The consequences in the higher corona were observed by UVCS and the Large Angle Spectrometric Coronagraph (LASCO) instrument on *SOHO*, as well as the Mauna Loa Solar Observatory's Mark IV K-Coronameter (MLSO MK4).

We were first impressed by this event in that the magnetic structures were severely stretched by the eruption and the two legs of the stretched structures soon started moving toward one another, approaching the presumed current sheet located between them. We were further impressed with the morphological features of the CME that developed during the eruption. Figure 2

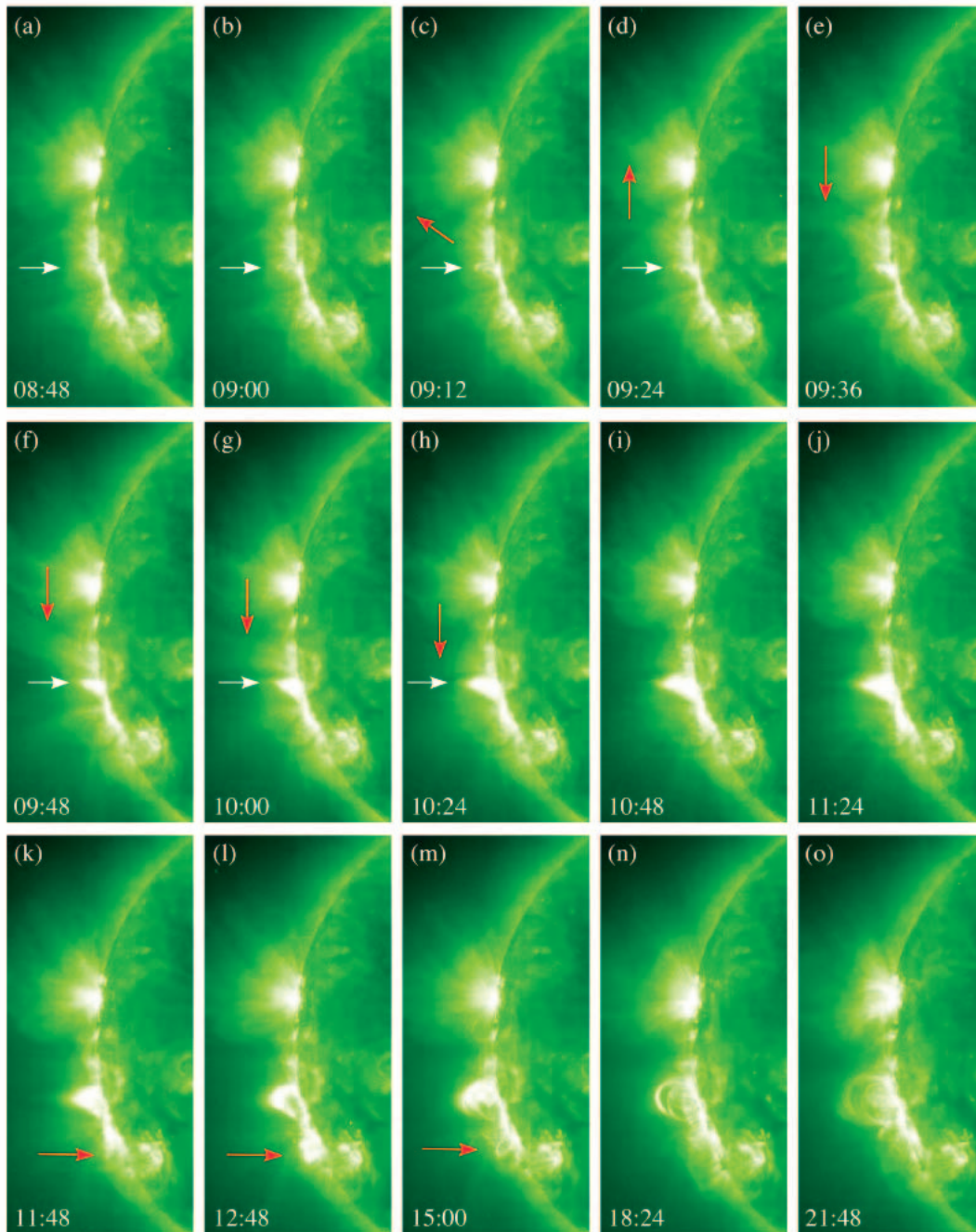


FIG. 2.—Set of EIT 195 Å images displaying the process that is characterized by the magnetic arcades' disruption, the driven magnetic reconnection, and the formation of flare loop system with a cusp structure on the top. The white arrows in (a) through (d) indicate the disrupting arcades, and the red arrows in (c) and (d) point in the direction of the arcade expansion and the arcade leg separation, respectively. The red arrows in (e) through (h) show the inflow of magnetic reconnection, and the white arrows in (f) through (h) indicate the cusp structure that forms right below the reconnection region. The field of view of each panel is  $0.27 R_{\odot} \times 0.59 R_{\odot}$ , and all times are UT. This figure is accompanied by more detailed mpeg animations in the electronic edition of the *Astrophysical Journal*.

displays a set of snapshots of the eruption during the initial phase observed in the 195 Å band by EIT; two accompanying mpeg animations are provided in the electronic version of the paper to depict more dynamical detail: one displays the apparent motions of the stretched magnetic structures near the presumed current sheet and the growing of the cusp point, and the other emphasizes the associated flare loops. Figure 3 shows the magnetic structures before and after the CME passed through the fields of view of the LASCO C2 and C3 coronagraphs. The snapshots in Figure 4 give more details of the CME and the subsequent evolutionary features observed by C2 (an accompanying ani-

mation in the electronic version illustrates more detailed morphological features), and Figure 5 is a composite of C2, UVCS, and EIT 195 Å images, which clearly manifests the objects at various altitudes developed in this major eruptive process. These objects bear a close similarity to the model shown in Figure 1.

The LASCO C2 images shown in Figures 4 and 5 have been enhanced by the wavelet technique, some details of which are provided and discussed below. We have arranged these figures in this fashion to provide the reader with the entire sequence of the eruption, as well as the key characteristics that we are focusing on in the present work. The relevant data, the tools we

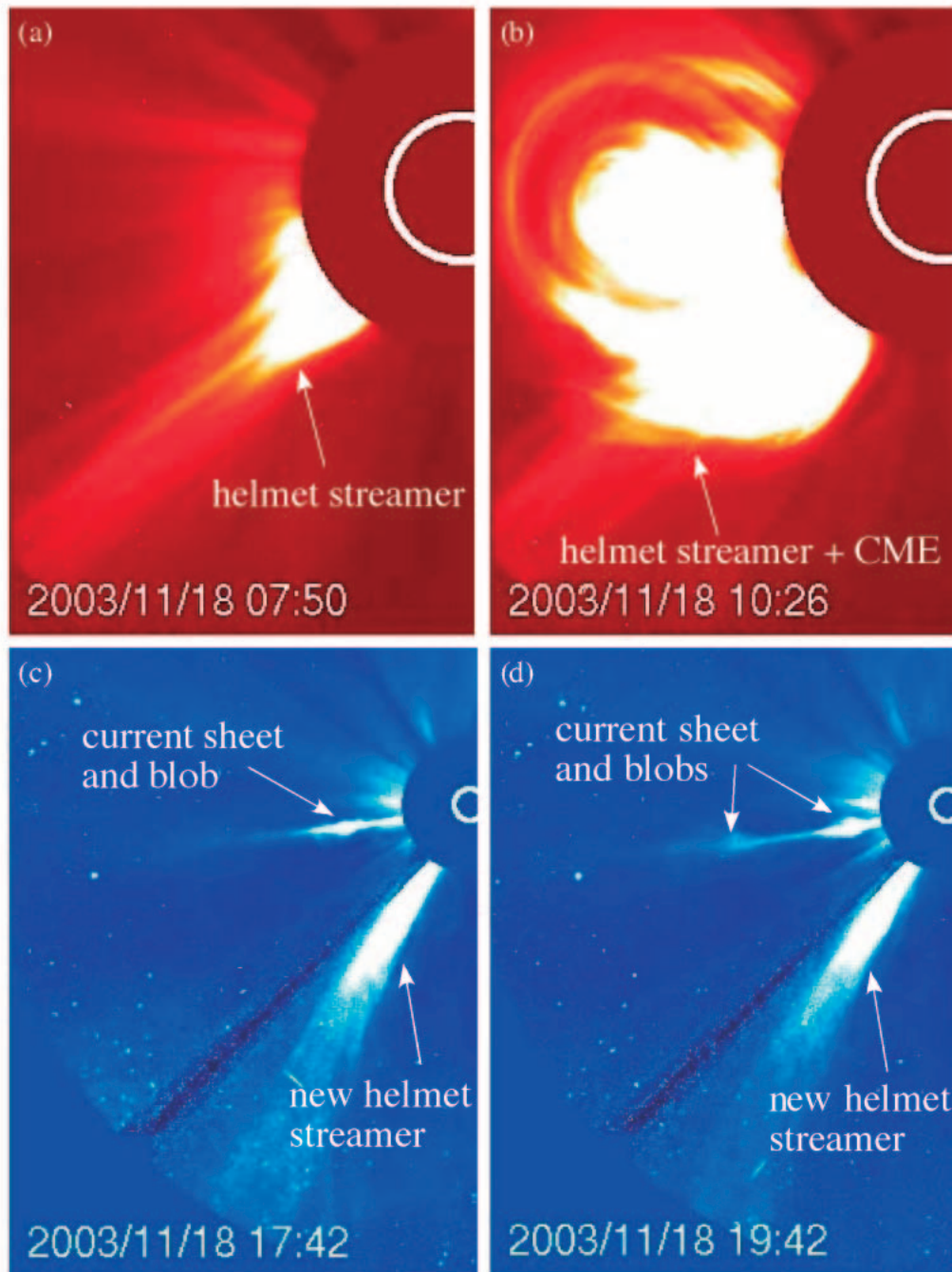


FIG. 3.—LASC0 C2 and C3 images. (a) A helmet streamer exists in the region that the CME will go through. With rapid expansion of the CME, (b) the helmet streamer is severely deflected from outside, and (c, d) the southern leg of the CME (disrupting arcade) merges with the helmet streamer, forming a new helmet streamer. A couple of blobs of the reconnected plasma flowing along the current sheet can also be recognized in (c) and (d). All times are UT.

used to process these data, and our detailed analysis and investigations are explained next.

### 2.1. EIT 195 Å, RHESSI Soft X-Ray, and MK4 White-Light Observations

The EIT 195 Å images taken in the time interval of interest have a field of view of  $1.4 R_{\odot} \times 1.4 R_{\odot}$  and a resolution of  $5''.3 \text{ pixel}^{-1}$ . Before the eruption took place, a group of bright arcades distributed at both sides of the equator could be seen clearly in the EIT 195 Å band. The EIT 195 Å sequence shows that the central arcade started to change at around 08:48 UT. A small, faint, arcade-like structure became distinguishable from the background (Fig. 2a). As it expanded outward, it split into three

small arcades, with the middle one being the brightest (Fig. 2b). The outer arcade exploded between 09:00 and 09:12 UT, and the middle one followed suit between 09:12 and 09:24 UT. The horizontal arrows in the relevant panels of Figure 2 indicate these arcades, and the red arrows indicate the direction of expansion. Along with the explosion of the middle arcade, two legs of the arcade system were quickly stretched out and separated from one another, with the northern one moving much faster than the southern one (Figs. 2c and 2d; note the red arrow). (The reasons for the different behavior of the two legs will be discussed shortly.) Then, these two legs began to approach one another at 09:36 UT (Fig. 2e; again note the red arrows in this and following panels), which implies an inflow of magnetic reconnection

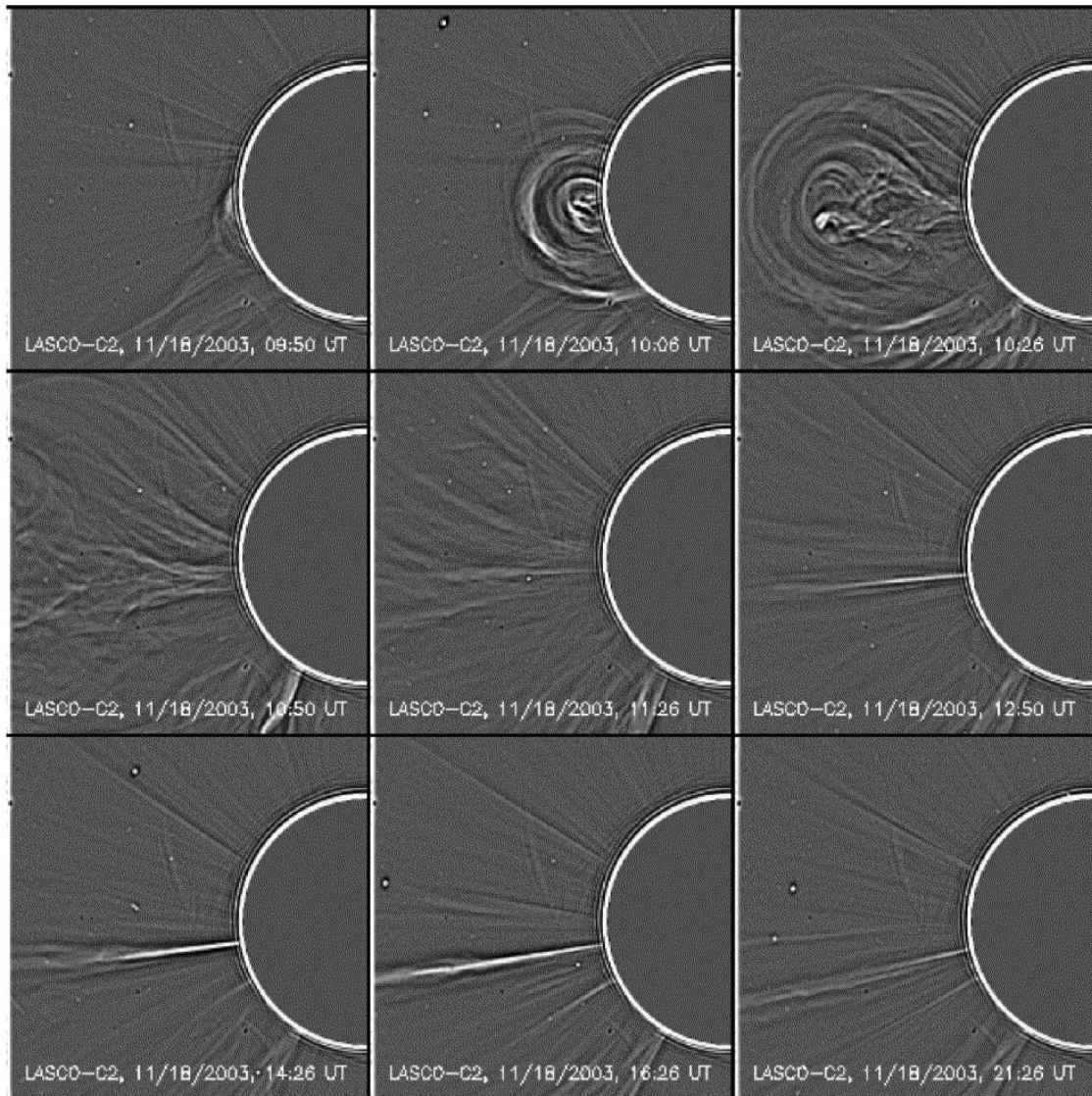


FIG. 4.—LASCO C2 images that have been enhanced by the wavelet technique, which is good at emphasizing the fine features of large-scale structures. The leading edge, cavity, and core of the CME, as well as the current sheet, are easily recognizable. This figure is also available as an mpeg animation in the electronic edition of the *Astrophysical Journal*.

driven by the eruption. Subsequently, a sharp, bright cusp structure formed and moved continuously upward (Figs. 2*f*–2*h*; note the white arrows). This process is quite similar to that in the eruption reported on by Yokoyama et al. (2001), which also showed an apparent reconnection inflow near the cusp point.

Following Yokoyama et al. (2001), we could measure the velocity at which the legs of the extended arcades approach one another and use it as the velocity of the magnetic reconnection inflow near the reconnection site (e.g., the X-type neutral point or the current sheet). However, the structure seen in the EIT images is diffuse, and an accurate speed is difficult to determine. Moreover, Chen et al. (2004) reanalyzed the observations of Yokoyama et al. and suggest that the apparent inward motion was actually due to the changing position of the X-type reconnection region rather than inflow. Therefore, we use the UVCS observations (see § 2.3), rather than the EIT images, to determine the inflow speed.

Around 11:24 UT, the top of the cusp structure started to become round, and its height also decreased (Figs. 2*j* and 2*k*), manifesting an apparent shrinkage process (see Svestka et al. 1987; Lin et al. 1995; Forbes & Acton 1996). The cusp structure then disappeared from the EIT field of view. In its place, a group

of bright flare loops appeared at successively higher altitudes (Figs. 2*k*–2*o*). The growth of flare loops observed in EIT 195 Å images lasted more than 20 hr, and the flare loops were still visible in the following days. The red arrows in Figures 2*k*, 2*l*, and 2*m* point to another flare loop system that started to form at around 11:48 UT (discussed below).

According to the standard theory of two-ribbon flares (see, e.g., Forbes & Acton 1996 and references therein), some fine structure in the magnetic field and plasma should exist between the cusp point and the postflare loops (Fig. 1). These features include a Mach 2 jet, a termination shock, condensation inflow, shock-enhanced cooling, and so on (see the lower half of Fig. 1). (We note that the Mach 2 jet is actually the reconnection outflow from the current sheet located above the cusp point, and that the Mach number here is the outflow speed compared with the Alfvén speed in the outflow region and not that in the inflow region, as used in most places in the present work.) Usually these features would not be distinguishable, because of either the lower resolution of the images or scattered light from the objects nearby. To look into these features, we applied the technique of wavelet-based intensity contrast enhancement (WICE) to process

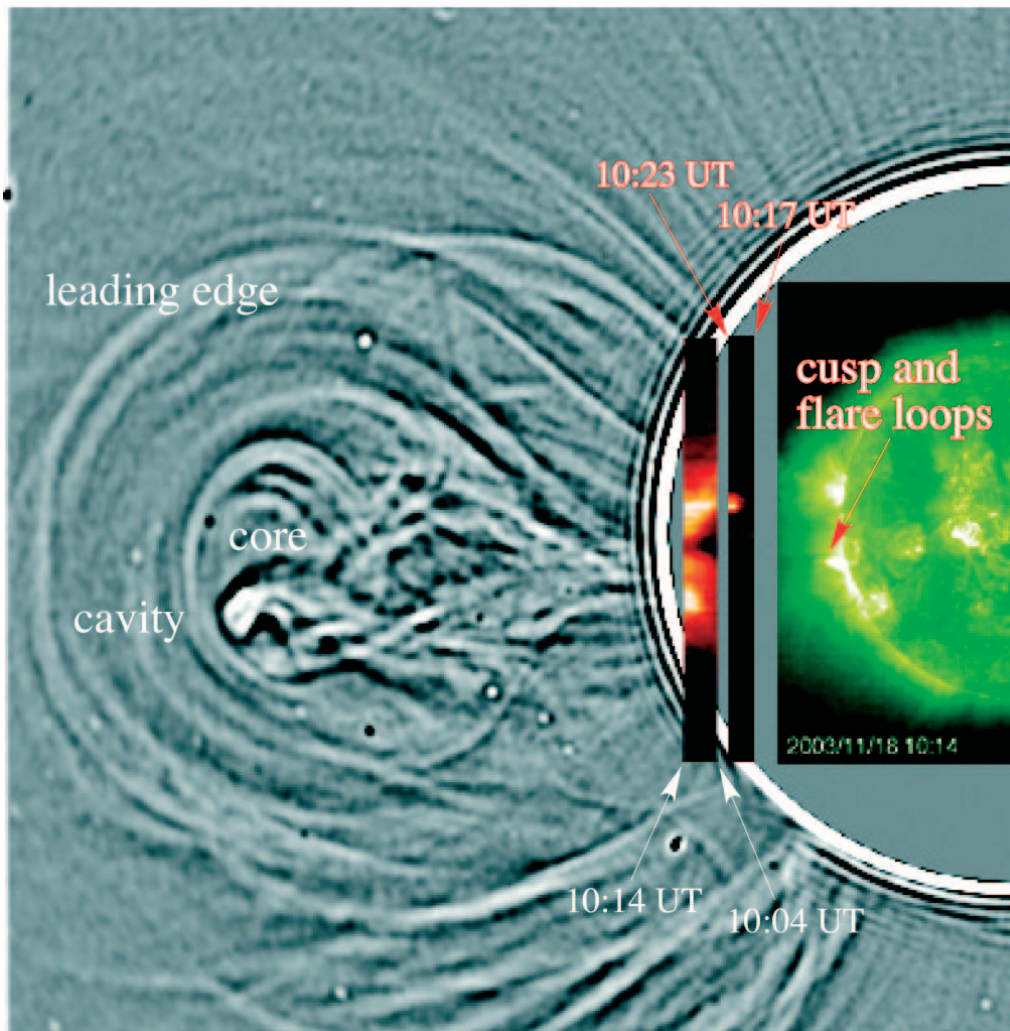


FIG. 5.—Composite C2-UVCS-EIT image. The C2 image was taken at 10:26 UT and has been enhanced by the wavelet technique in order to emphasize the morphological features at various positions of the CME, the EIT 195 Å image was taken at 10:14 UT, the left UVCS image was made by stacking five UVCS exposures in Ly $\alpha$  that were taken at an altitude of 1.70  $R_{\odot}$  and cover the time interval from 10:04 UT (right edge) to 10:14 UT (left edge), and the right UVCS image was made by stacking four UVCS exposures in Ly $\alpha$  that were taken at an altitude of 1.52  $R_{\odot}$  and cover the time interval from 10:17 UT (right edge) to 10:23 UT (left edge).

the images in Figure 2. Detailed descriptions and discussions of this technique can be found in works by Starck et al. (1997) and by Stenborg & Cobelli (2003). The advantage of the images obtained this way is that the small-scale features of a magnetic field embedded within large-scale structures can be enhanced significantly.

The enhanced EIT images do not show significant differences at large scales from those in Figure 2, but the flare loops below the cusp region are now visible from 10:24 UT (see Fig. 6, left), when the cusp structure is still visible in the EIT 195 Å images. The apex of the loop system is not right beneath the cusp point. Instead, they are separated by a distance of around  $6.5 \times 10^4$  km. This distance was not constant but increased with time (see the other three panels of Fig. 6). In the panels taken at 10:24, 10:36, and 11:00 UT, we also note a short, bright stemlike feature between the cusp point and the top of the flare loops. This feature exists for about an hour, from 10:14 to 11:12 UT, and is brightest within the interval between 10:24 and 11:00 UT. Furthermore, a faint looplike gap exists between the lower tip of this feature and the top of the bright EIT 195 Å loops (see the two left panels in Fig. 6). Comparing the details shown in Figure 1, we find that this feature is located just where the Mach 2 reconnection jet and the termination shock should appear, and that the faint looplike gap seen in the enhanced EIT 195 Å images is probably the position

where the hot ( $\sim 10^7$  K) soft X-ray loops, together with the shock-enhanced cooling, should sit according to the standard model for two-ribbon flares (see also Forbes & Malherbe 1986; Forbes & Acton 1996). More dynamical details of the above process can be seen clearly in the animations mentioned above.

In addition to the EIT 195 Å observations, the cusp structure was observed by *RHESSI*. The tip of the cusp in the *RHESSI* images was about  $7 \times 10^4$  km above the limb (Fig. 7). The two *RHESSI* images used in this work were obtained within the time interval from 09:37 to 10:23 UT. The early rising phase of the event was missed because of the South Atlantic Anomaly and Earth eclipse (*RHESSI*'s nighttime). The soft X-rays ( $< 25$  keV) peaked around 10:00 UT. No apparent hard X-ray emission ( $> 25$  keV) was observed. But the *RHESSI* images at energies below 25 keV clearly show a looplike structure, and those in the 12–16 keV channel observed between 09:39 and 10:05 UT obviously display a cusp structure on the top of the flare loops. Two such images are overlaid on an EIT 195 Å image in Figure 7. The field of view of these two images is about  $200'' \times 200''$ . The cusp feature observed in X-ray emission is clearly spatially coincident with that in seen by EIT at 195 Å.

After the cusp structure disappeared from the EIT field of view, it could still be seen at higher altitudes, as shown in the MLSO

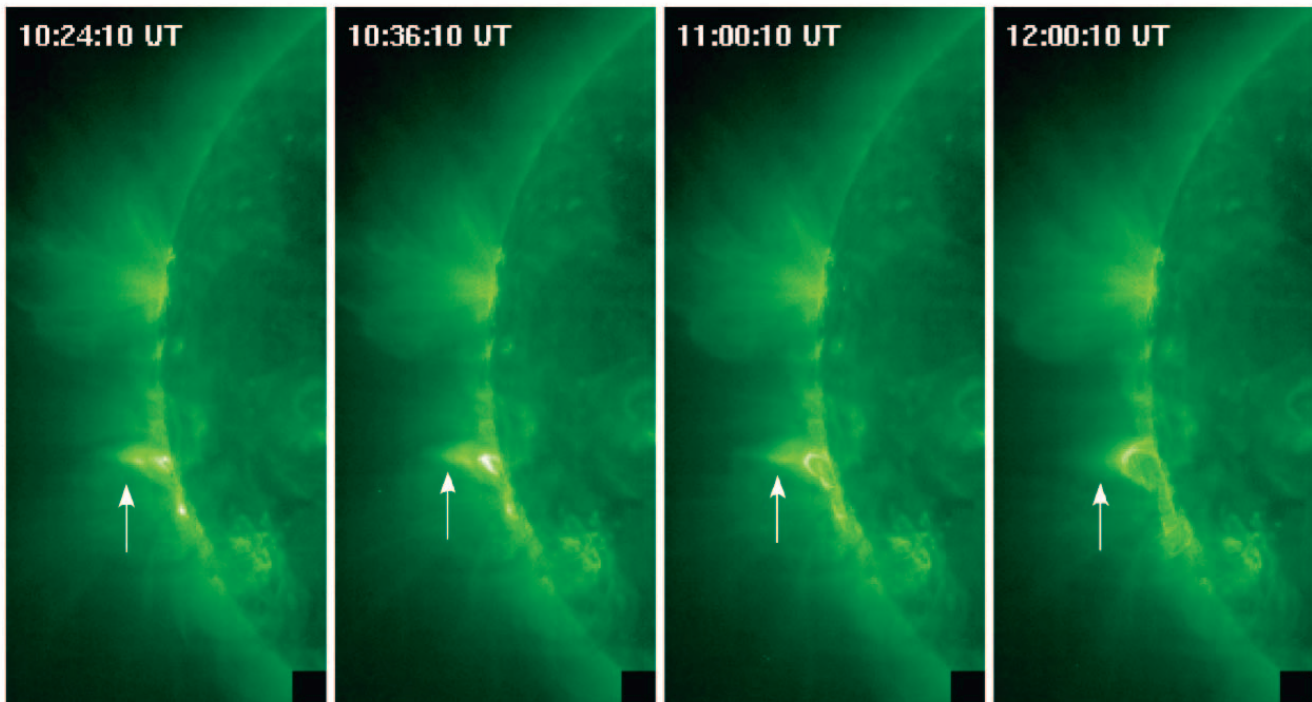


FIG. 6.—EIT 195 Å images that have been processed with the WICE technique. Compared with the corresponding images in Fig. 2, these show more details of the fine structures between the cusp point and the flare loops. The field of view of each panel is  $0.27 R_{\odot} \times 0.59 R_{\odot}$ .

MK4 white-light images. Figure 8 is a composite of LASCO C2 (at 17:50 UT), MK4 (17:49 UT), and EIT 195 Å (17:48 UT) images, clearly illustrating the positions of the post-flare/CME loops, cusp point, and extended current sheet. Figure 8 obviously resembles the typical Kopp-Pneuman configuration for major flares (see Kopp & Pneuman 1976; Forbes & Acton 1996; references therein), in which the post-flare/CME loops are located under the cusp structure at the lower tip of the current sheet and the upper tip of the current sheet extends to a large distance.

## 2.2. Observations by LASCO C2 and C3

Prior to the event, a helmet streamer was present at a position angle (P.A.) of about  $135^{\circ}$  (Fig. 3a), measured counterclockwise from solar north. Comparison with the  $H\alpha$  and MDI images suggests that it was located over either AR 0506 or AR 0508. Following the explosion observed by EIT at 195 Å, the front of a fast CME appeared in the field of view of LASCO C2 at 09:26 UT and in that of LASCO C3 at 10:42 UT, showing a typical three-component CME structure with a large, bright core (Fig. 3b). According to the *SOHO* LASCO CME Catalog,<sup>5</sup> it was a partial-halo CME with angular width in excess of  $197^{\circ}$ . The motion of the CME core remains in the plane of P.A. =  $96^{\circ}$ , which is very close to the equatorial plane.

### 2.2.1. The CME in the LASCO Field of View

A comparison of Figure 3a with Figure 8 indicates that the helmet streamer was located very close to the region where the eruption took place. An interaction between the magnetic field involved in the eruption and that of the helmet streamer may be expected. With the data we were able to collect, we lack direct evidence of the interaction. However, such an interaction can be conjectured on the basis of the following observational facts: The existence of the helmet streamer tends to prevent the

eruptive arcades from moving southward (Fig. 2c, red arrow), which suggests that the magnetic fields in both structures have the same orientation but belong to two different magnetic systems without a topological connection. Interaction with the helmet streamer also tends to push the CME to propagate northward. With the magnetic field in the helmet streamer getting weaker at higher altitudes and with the rapid expansion of the CME bubble, however, the helmet streamer was deflected toward the south (Fig. 3b). The deflection was so severe that the oppositely oriented magnetic fields in the helmet streamer were driven to reconnect with one another. The EIT 195 Å animation indicates that the reconnection occurred at around 12:24 UT, with the newly formed flare loops located south of those developing earlier as the signature. (The reader may consult the image sequence available on the *SOHO* Web site, or compare the details of the bright features indicated by the red arrows in Figs. 2l and 2m.) Subsequently, the southern leg of the CME (disrupting arcade) merged with the northern leg of the helmet streamer and formed a new helmet streamer (Figs. 3c and 3d), which looks like the old one. This is different from cases in which CMEs blow away helmet streamers from inside (see, e.g., Raymond et al. 2003 and references therein).

Meanwhile, the interaction caused the evolution of the CME's morphological structures to be very nonuniform as well. Figure 9 displays the height-time profiles at three different CME positions, as well as the deduced velocities and accelerations. The leftmost panels in Figure 9 show the results for the CME core measured at P.A. =  $96^{\circ}$ . The top panel plots the height versus time. The circles give the observed data, and the curve shows the result of a fit based on the following formula:

$$h(t) = a_1 + a_2 t + a_3 t^2 e^{-a_4 t}, \quad (1)$$

where  $a_1$  through  $a_4$  are the fit coefficients,  $h$  is the height in kilometers,  $t$  is the time in seconds, and we set 09:00 UT as

<sup>5</sup> See [http://cdaw.gsfc.nasa.gov/CME\\_list/](http://cdaw.gsfc.nasa.gov/CME_list/).

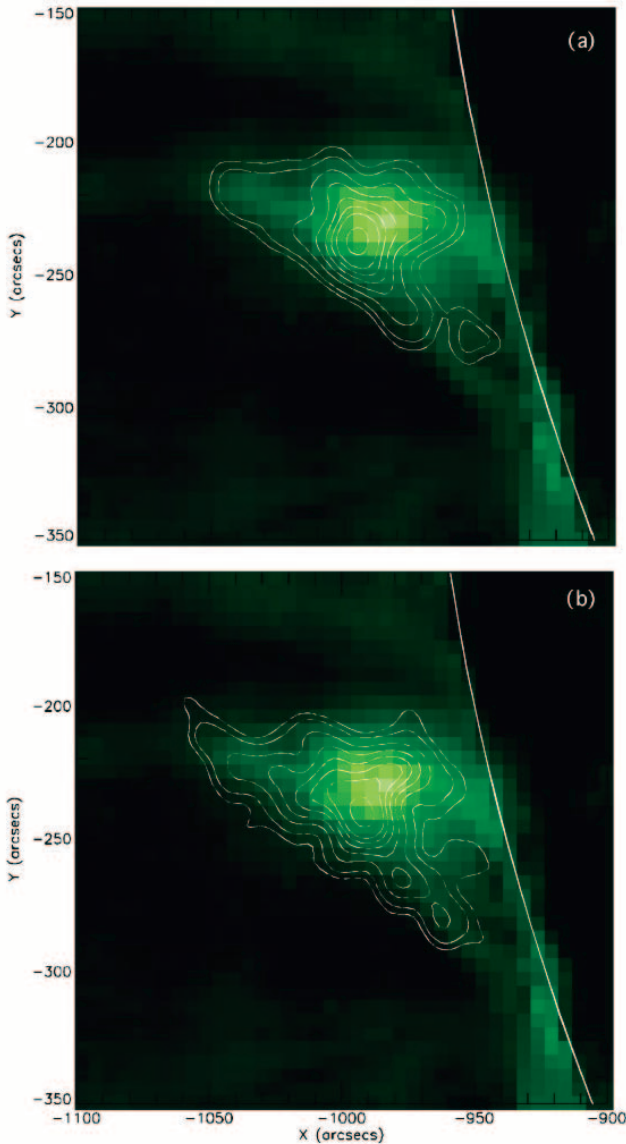


FIG. 7.—Two *RHESSI* 12–16 keV images (contours), showing the cusp feature over the flare loop system, overlaid on the nearest *EIT* 195 Å image. The *RHESSI* contours in (a) were taken at 09:59 UT and those in (b) were taken at 10:02 UT. The contour levels in each image are 15, 20, 30, 40, 50, 60, 70, 80, and 90 percent of the peak intensity. The *EIT* 195 Å images in both panels were taken at 10:00 UT.

$t = 0$  when doing the curve fitting. The corresponding velocities  $dh/dt$  and accelerations  $d^2h/dt^2$  are then deduced from equation (1), and they are plotted versus time in the two lower panels (Fig. 9a). The first row of Table 1 lists  $a_1$  through  $a_4$  and the maximum velocity  $v_{\max}$ , as well as the corresponding time  $t_{\max}$  and height  $h_{\max}$  for the CME core as measured at P.A. =  $96^\circ$ . The nonuniform expansion of the CME bubble can be investigated by tracking some points on its leading edge. We choose two points, located at P.A. =  $88^\circ$  and P.A. =  $100^\circ$ , on the leading edge. Two sets of data for height versus time were obtained. We plot these in the top middle and right panels of Figure 9, respectively, along with fits to the curve described by equation (1). The corresponding velocities and accelerations are plotted in the panels beneath. The fit coefficients, together with the maximum velocities and corresponding time  $t_{\max}$  and height  $h_{\max}$  deduced from equation (1), are listed in the second and third rows of Table 1.

More details of the CME's morphological features can be discerned in the enhanced C2 images. Figure 4 displays a set of

such images that have been processed using the WICE technique. These cover the time interval from 09:50 to 21:26 UT. The fine structures that we highlight include the leading edge and core of the CME (see the images at 10:06 and 10:26 UT), the characteristics of the magnetic field around the current sheet (images at 10:50 and 11:26 UT), and the current sheet itself (images at 12:50, 14:26, 16:26, and 21:26 UT). From this set of images, one may also clearly see the helmet streamer at P.A. =  $135^\circ$  being deflected from outside by the CME by comparing the 09:50 UT image with the others. The helical structure around the CME core is also worth noting (images at 10:06 and 10:26 UT in Fig. 4). It appears to show the shape of a flux rope surrounded by a bubble (see, e.g., Lin et al. 2004). The reader may find more information by watching the corresponding animation mentioned in § 2.

### 2.2.2. Reconnection Outflow along the Current Sheet

Following the tangled structure of the CME, a long, thin streamer-like feature appeared in the field of view of *LASCO* C2 and then C3, and several bright blobs successively flowed away from the Sun along this feature (see Figs. 3c and 3d). This thin streamer-like structure initially appeared at P.A. =  $90^\circ$  and moved slowly toward the south, approaching P.A. =  $116^\circ$ , which suggests a process of self-adjustment in the disrupted magnetic field as the eruption progressed. During this process several blobs are recognizable, and we investigated the motions of five of them with good resolution. The heights of these five are plotted versus time in Figure 10, and the curves were fitted to the data on the basis of the following quadratic relation:

$$h(t) = b_1 + b_2t + b_3t^2, \quad (2)$$

where  $h$  is in kilometers,  $t$  is in seconds, and the time shown at the lower left of each curve in Figure 10 is set to  $t = 0$  for the corresponding blob. The values of these coefficients are listed in Table 2 for each of the five blobs. The motion of blob 1 manifested an apparent acceleration of  $158 \text{ m s}^{-2}$ , that of blob 2 showed a deceleration of  $42.5 \text{ m s}^{-2}$ , and the other three moved with a slight acceleration varying from  $16.7$  to  $26.7 \text{ m s}^{-2}$ . We also calculated the average velocities for all five blobs, which are listed in the last column of Table 2. It is interesting that blob 1 showed the largest acceleration although its average speed was the lowest ( $460 \text{ km s}^{-1}$ ); on the other hand, blob 2 decelerated and had the highest average speed ( $1075 \text{ km s}^{-1}$ ). From the times shown in Figure 10, we also note that magnetic reconnection associated with this event was still in progress after 21:00 UT on 2003 November 19. This implies that the entire event lasted for more than 36 hr, which is typical of a long-duration event.

Having compared the above process and characteristics displayed by the thin streamer-like structure shown in Figures 3 and 8 with those displayed by the developing current sheet investigated by Ko et al. (2003), we believe that the thin structure in the present case is also a current sheet developing in the wake of the CME, and that the blobs in the outflow are due to magnetic reconnection inside the current sheet. The change in the velocity of those blobs suggests that the current sheet was not uniform and that the rate of magnetic reconnection varied with time and position.

### 2.3. UVCS Observations

During the observations described above, the UVCS instrument also observed this CME during one of its synoptic scans. At 10:04 UT, the UVCS slit was placed at  $1.70 R_\odot$  at P.A. =  $90^\circ$  and five 120 s exposures were acquired (see the left UVCS

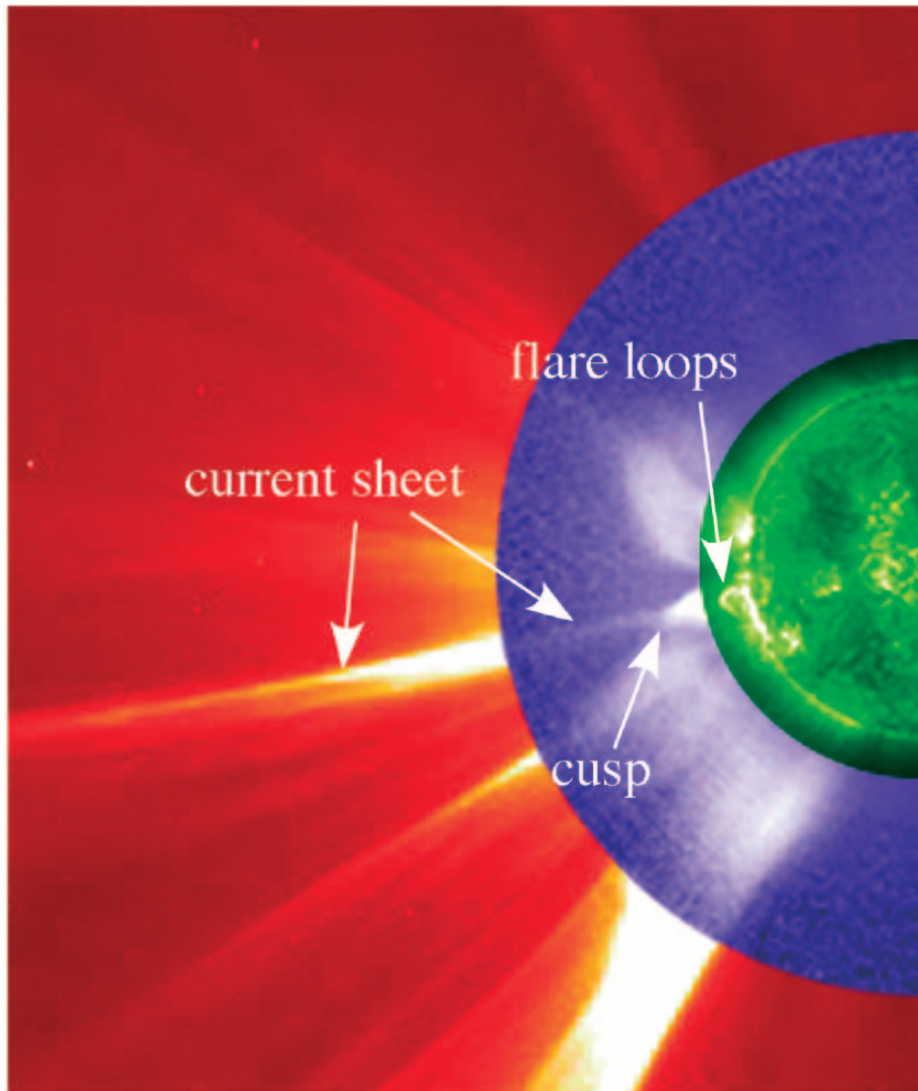


FIG. 8.—Composite of C2 (at 17:50 UT), MK4 (17:49 UT), and EIT 195 Å (17:48 UT) images. The cusp structure is clearly seen in the MK4 white-light image at the lower tip of the current sheet, and a group of flare loops seen in the EIT 195 Å image is located right below the cusp point. At this time, the CME has been out of the field of view for a while. The field of view of the MK4 image is  $2.76 R_{\odot} \times 5.45 R_{\odot}$ .

image in Fig. 5). The corresponding Ly $\alpha$  intensity distributions along the slit are shown in Figure 11a. The slit was then moved to  $1.52 R_{\odot}$  and four more exposures were taken (see the right UVCS image in Fig. 5); the Ly $\alpha$  intensity distributions are given in Figure 11b.

The data reported here were taken from the O VI channel. The slit width was set to  $150 \mu\text{m}$ , which corresponds to an instantaneous field of view of  $40' \times 42''$ . The synoptic data were obtained with a spatial binning of 3 pixels ( $21''$ ) and a spectral binning of 2 pixels ( $0.183 \text{ \AA}$  for Ly $\alpha$ ). The raw data have been wavelength- and flux-calibrated. The uncertainty in the flux calibration is about 20% for the first-order lines (Gardner et al. 2000). Stray light is negligible in the data, so no stray-light correction has been performed.

Figure 5 is a composite of a C2 image at 10:26 UT that has been enhanced by the WICE technique, an EIT image at 10:14 UT, and two images of the UVCS slit located at  $1.70$  and  $1.52 R_{\odot}$ , respectively. The UVCS image to the left was created by stacking five exposures of the Ly $\alpha$  intensity distributions along the UVCS slit taken at  $1.70 R_{\odot}$ , which covers the time interval from 10:04 to 10:14 UT; that to the right was

created by stacking four exposures of the Ly $\alpha$  intensity distribution along the UVCS slit taken at  $1.52 R_{\odot}$ , which covers the time interval from 10:17 to 10:23 UT. So, the horizontal scale of the UVCS images does not represent the extension in space, but in time. Comparing with those at the corresponding times shown in Figure 2, one can easily find that the dark gap in the UVCS image at early times coincided with the separating motions of the two legs of the eruptive arcades in both space and time, and that this gap gradually disappeared as a result of the reconnection inflow near the current sheet. The process in which the gap disappears can also be seen from the changes in the profiles of Ly $\alpha$  intensity shown in Figure 11a. Its importance as a velocity diagnostic will be investigated below.

During the four exposures at  $1.52 R_{\odot}$ , the gap was barely visible, but a bright feature was apparent at a position angle of  $88^{\circ}$  (see the right UVCS image in Fig. 5 and the curves in Fig. 11b). This feature brightened rapidly, from  $3.8 \times 10^{11} \text{ ergs cm}^{-2} \text{ s}^{-1} \text{ sr}^{-1}$  between 10:16 and 10:18 UT to  $1.4 \times 10^{12} \text{ ergs cm}^{-2} \text{ s}^{-1} \text{ sr}^{-1}$  between 10:20:26 and 10:22:34 UT in Ly $\alpha$ . It was visible in low-temperature lines: H I Lyman, C III  $\lambda 977$ ,

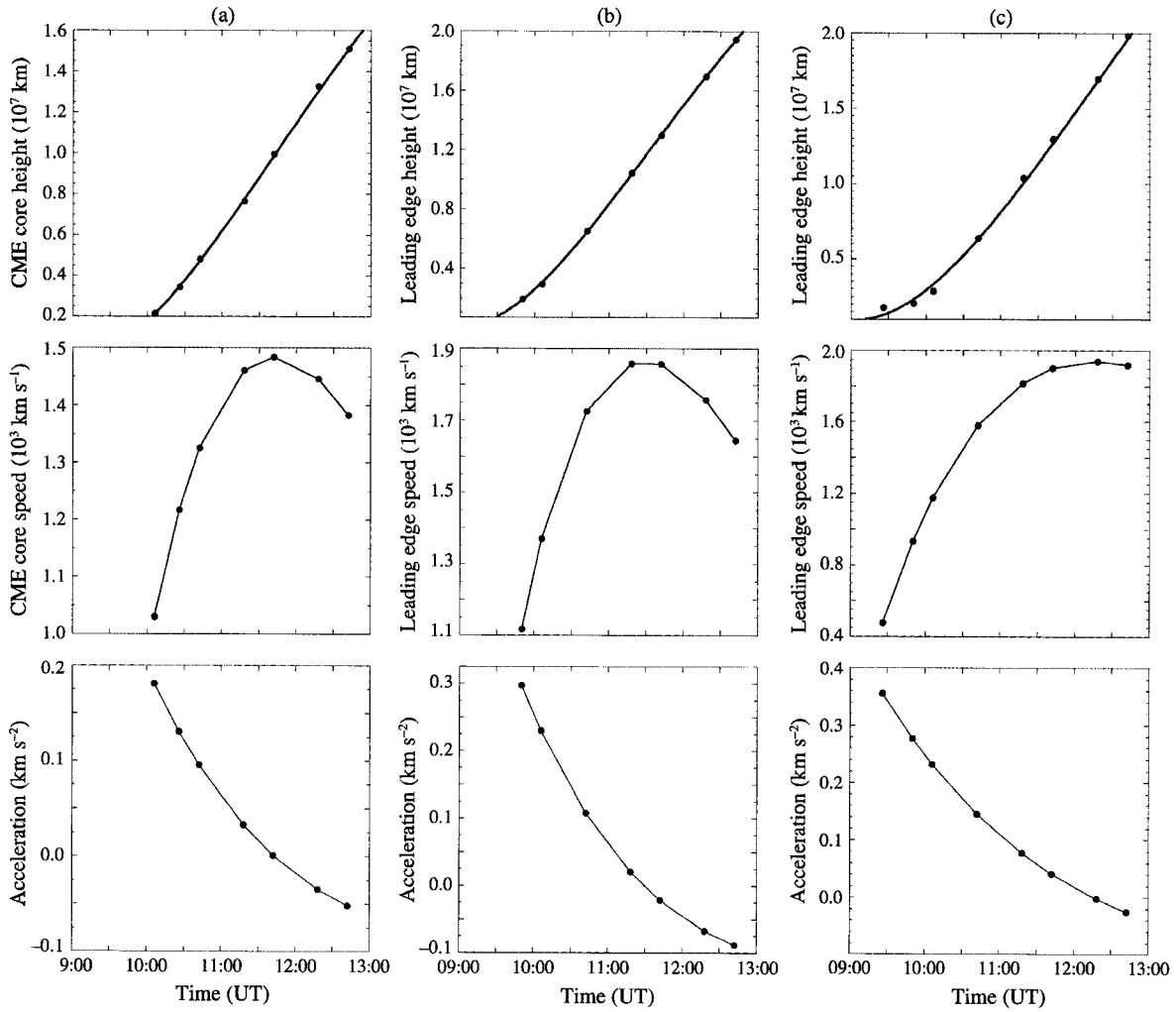


FIG. 9.—Variation of heights, velocities, and accelerations of various points on the CME bubble: (a) the CME core at P.A. = 96°; (b) the CME leading edge at P.A. = 88°; (c) the leading edge at P.A. = 100°.

N III  $\lambda 991$ , O VI  $\lambda\lambda 1023, 1037$ , and Si III  $\lambda 1206.5$ . The bright feature was about 10 times as bright as neighboring regions in Ly $\alpha$ , but only about twice as bright in O VI. We do not have a reliable density diagnostic in this case, but the brightening can easily be accounted for by lower temperature plasma spanning the range  $7 \times 10^4$  to  $3 \times 10^5$  K with a density similar to that in adjacent regions along the slit. We interpret the low-temperature feature as material in one of the CME legs, which is often visible in UVCS observations as sharp features seen in cool lines for a long time (Ciaravella et al. 2000).

2.3.1. Velocity Diagnostic

The above process of dimming and recovery observed in Ly $\alpha$  by UVCS is also important for the diagnosis of the magnetic reconnection inflow velocities near the current sheet. The spatial distributions of the Ly $\alpha$  intensities along the UVCS slit

shown in Figure 11a manifest an apparent low-emission area. This area corresponds to the dark gap seen in the left UVCS image in Figure 5 and existed at around P.A. = 95°, indicating coronal dimming as a result of the eruption. The width of this gap decreased with time, indicating the inflow of magnetic reconnection and the coincidence of the current sheet with the gap in space. Comparing the widths of the gap every two successive times helps one to deduce the velocities of the reconnection inflow,  $V_R$ . Five Ly $\alpha$  intensity profiles yield four values of  $V_R$ : 73.2, 106, 36.6, and 10.5 km s $^{-1}$ . Strictly speaking, these are the average values over four periods: 10:04:15–10:06:45 UT, 10:06:45–10:09:13 UT, 10:09:13–10:11:41 UT, and 10:11:41–10:14:11 UT (Fig. 11a). Comparing these velocities with the local Alfvén speed,  $V_A$ , in the reconnection inflow region yields the rate of magnetic reconnection in terms of the inflow Alfvén Mach number,  $M_A$ , namely,  $M_A = V_R/V_A$ .

TABLE 1  
COEFFICIENTS  $a_i$  FOR EQUATION (1) AND OTHER PARAMETERS

Object	$a_1$ ( $\times 10^5$ )	$a_2$ ( $\times 10^2$ )	$a_3$ ( $\times 10^0$ )	$a_4$ ( $\times 10^{-5}$ )	$v_{\max}$ (km s $^{-1}$ )	$t_{\max}$ (UT)	$h_{\max}$ ( $10^6$ km)
CME core at P.A. = 96° .....	0.41	−1.13	0.21	4.00	1484	11:43	9.95
Leading edge at P.A. = 88° .....	2.23	−1.69	0.29	6.55	1865	11:29	11.57
Leading edge at P.A. = 100° .....	9.90	−1.53	0.23	5.00	1939	12:15	16.54

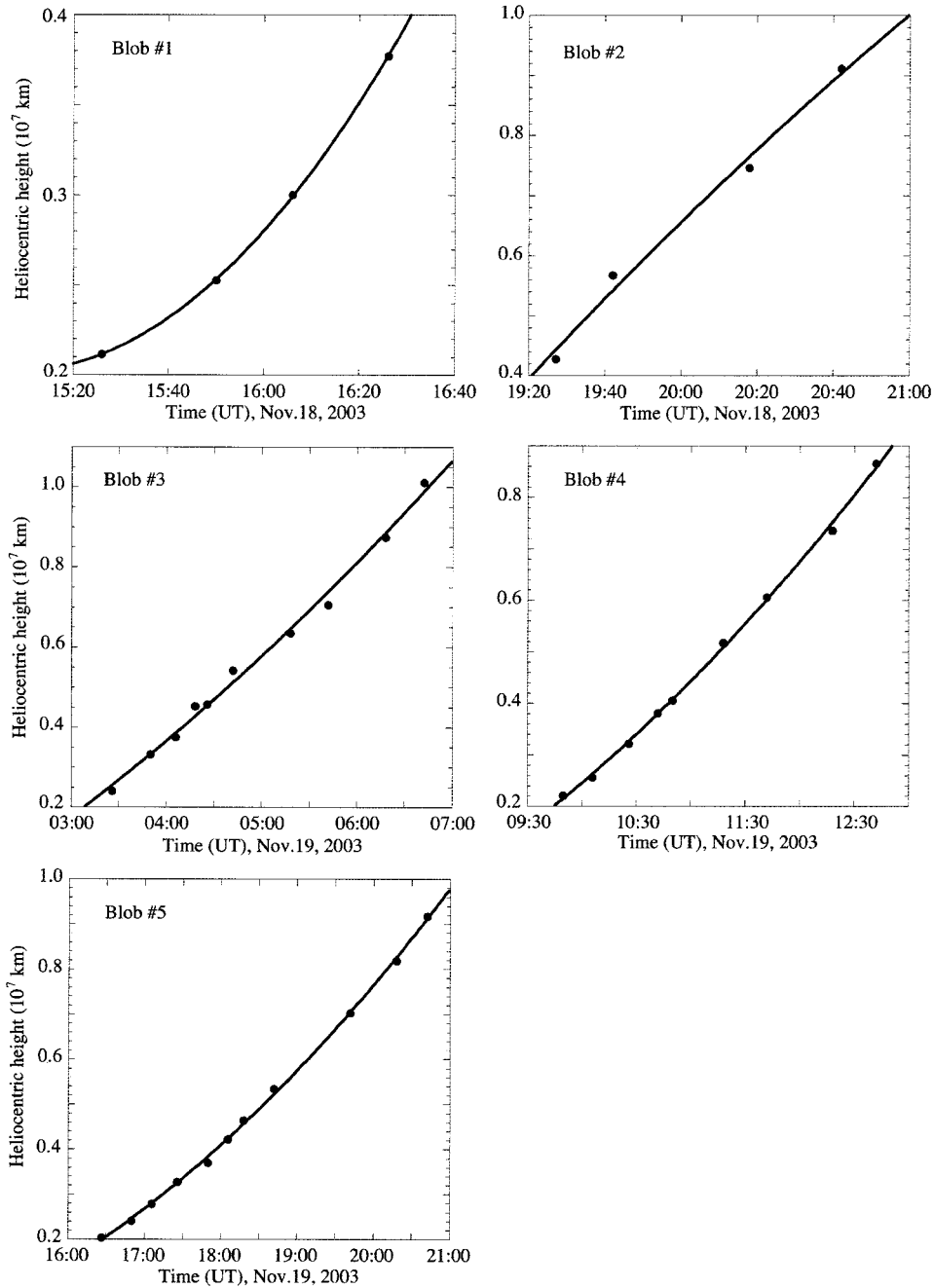


FIG. 10.—Height vs. time for five blobs. The circles are observational data, and the curves are drawn according to eq. (2) with the coefficients given in Table 2.

In the present case, we have identified the blobs as magnetic reconnection outflows along the current sheet. According to the standard theory of magnetic reconnection (see, e.g., Priest & Forbes 2000), the velocities of the blobs are either equal to  $V_A$  if the plasma is incompressible or differ from  $V_A$  by a factor of the

square root of the plasma density of the inflow region compared with that of the outflow region. In reality, the plasma is compressible, but numerical experiments indicate that the above factor varies between 1 and 2 in the coronal environment (e.g., Forbes & Malherbe 1986). So, an incompressible plasma is a good

TABLE 2  
COEFFICIENTS  $b_i$  FOR EQUATION (2)

Blob	$b_1$	$b_2$	$b_3$	Acceleration ( $\text{m s}^{-2}$ )	Average Speed ( $\text{km s}^{-1}$ )
1.....	$4.05 \times 10^7$	$-3.49 \times 10^3$	$7.91 \times 10^{-2}$	158	460
2.....	$-6.82 \times 10^7$	$2.74 \times 10^3$	$-2.15 \times 10^{-2}$	-42.5	1075
3.....	$-2.66 \times 10^6$	$3.17 \times 10^2$	$8.39 \times 10^{-3}$	16.7	655
4.....	$8.10 \times 10^5$	$4.05 \times 10^2$	$1.34 \times 10^{-2}$	26.7	573
5.....	$1.49 \times 10^5$	$2.93 \times 10^2$	$9.23 \times 10^{-3}$	18.5	465

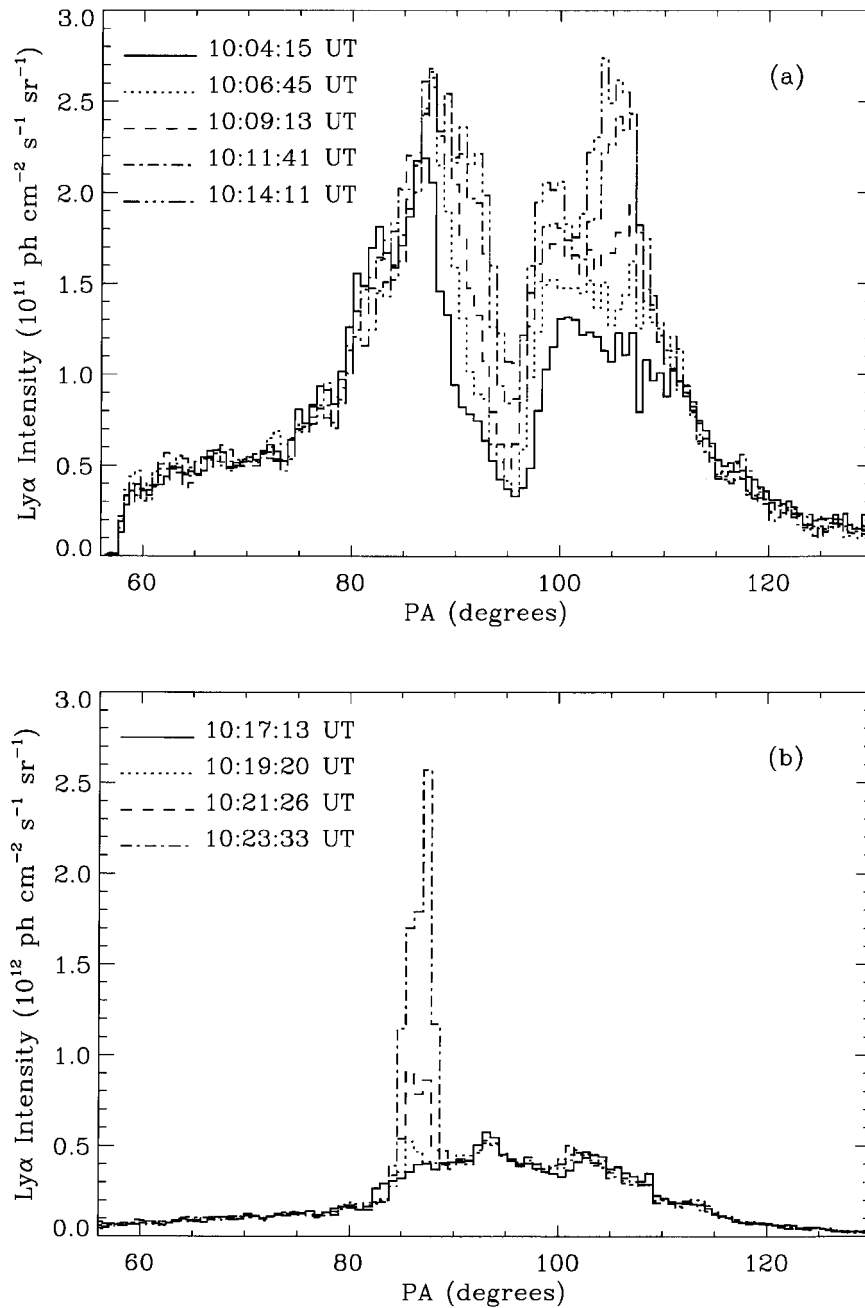


FIG. 11.—(a) Five Ly $\alpha$  intensity profiles along the UVCS slit taken at  $1.70 R_{\odot}$  from 10:04 to 10:14 UT. The dip in each profile is suggestive of the dark gap shown in Fig. 5. The decrease in the depth of the dip or the gap size results from the inflow of the driven magnetic reconnection caused by the eruption at the early stage. (b) Four Ly $\alpha$  intensity profiles along the UVCS slit taken at  $1.52 R_{\odot}$  from 10:17 to 10:23 UT. A bright feature appears at P.A. =  $88^{\circ}$  and brightens rapidly.

approximation for the processes occurring in the corona. This therefore gives values of  $M_A$  in the range from 0.01 to 0.23. In principle,  $M_A$  is a function of both space and time, as well as of the parameters for the current sheet, such as the length scale and the resistivity. However, there is no theory that describes rigorously how  $M_A$  depends on these parameters, especially when the eruption is in the phase of rapid evolution. Hence, what we can say about our results for the time being is that the real value of  $M_A$  in the present case should vary over a wider range than that deduced above, because our calculations are based on the average values of both  $V_R$  and  $V_A$ .

### 2.3.2. Temperature Diagnostic

To further confirm that the dark gap in the UVCS images is the region where the current sheet is located, we also looked into the

properties of other spectral lines. Generally, such a dark gap in UVCS images could correspond to the traditional EIT dimming (Harrison et al. 2003; Thompson et al. 2000; references therein), which results from severe stretching of the disrupted magnetic field and the consequent transient depletion of the plasma density. However, because the Ly $\alpha$  intensity depends on the H I neutral fraction and on Doppler dimming, the gap could result from a higher temperature or a significant outflow speed.

Figure 12 shows three Ly $\alpha$  profiles averaged over the five exposures at  $1.70 R_{\odot}$  in the gap and at positions to the north and south. We note that the existence of the gap does not necessarily mean that the emission from this region vanishes; instead, it just implies that the emission from this region is lower than that from the regions nearby. In the average profiles, the Ly $\alpha$  width in the gap is considerably larger than in the regions to the north

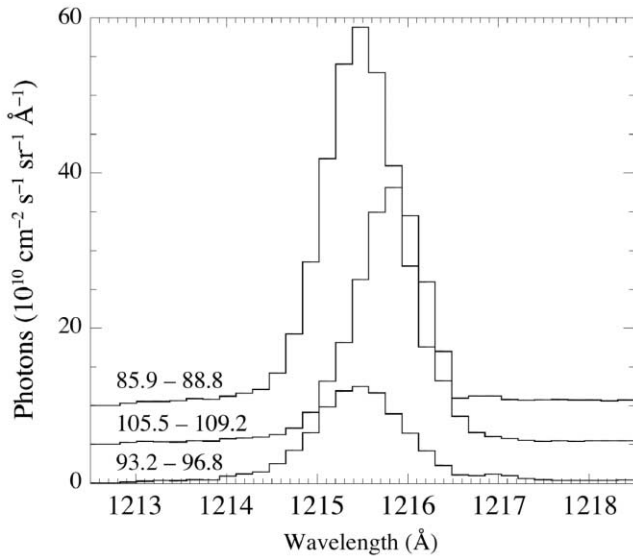


FIG. 12.—Three Ly $\alpha$  intensities as functions of wavelength averaged over different P.A. ranges, indicated by each pair of numbers on the corresponding profile: The curve labeled “93.2–96.8” is for the gap, “85.9–88.8” is the region north of the gap, and “105.5–109.2” is the region to the south. These Ly $\alpha$  profiles were taken at  $1.70 R_{\odot}$  and also averaged over the time interval from 10:04 to 10:14 UT.

and south, suggesting higher temperature. However, the individual exposures show that the Ly $\alpha$  line width measured at the center of the gap (P.A. = 93.2–96.8) decreases from 2.24 Å (FWHM) during the first exposure to 1.25, 1.18, 1.12, and 1.06 Å in the subsequent exposures. This can be compared with a line width of 1.09 Å south of the gap. If the line width were taken as the thermal width, the temperature in the gap would be  $6.7 \times 10^6$  K in the first exposure. However, a temperature this high would require a density above  $10^8 \text{ cm}^{-3}$  to account for the Ly $\alpha$  intensity, and this would imply an easily detectable signal in the [Fe xviii] 974.8 Å line. Therefore, we conclude that the low Ly $\alpha$  intensity is not due to high temperature but to either a smaller density or Doppler dimming (Noci et al. 1987 and references therein). An outflow speed of  $200 \text{ km s}^{-1}$  would account for the low intensities in the gap if the densities were similar to those outside of it. The large line width in the first exposure could then be attributed to the line-of-sight component of the outflow. Because we identify the gap with the feature seen as a modest density enhancement in the LASCO images at greater heights, we believe that Doppler dimming is the explanation for the low emission.

In principle, either the gap seen at  $1.70 R_{\odot}$  or the cool region seen at  $1.52 R_{\odot}$  might be associated with the bright ray seen by LASCO about an hour later. Based on the  $96^{\circ}$  position angle of the LASCO filament, the position of the gap at  $1.70 R_{\odot}$  ( $96^{\circ}$ ) and the cool plasma at  $1.52 R_{\odot}$  ( $87^{\circ}$ ), the ray seen in white light is associated with the Ly $\alpha$  gap, while the cool material farther north is associated with the fainter, more diffuse material seen in Figure 8 just north of the equator. While it seems counterintuitive to identify a bright feature in white light with a dark feature in Ly $\alpha$ , a substantial outflow speed is common to both.

It is also worth noting that the Ly $\alpha$  profiles to the north and south of the gap are shifted with respect to the centroid of the Ly $\alpha$  profile in the gap by about  $-20$  and  $+35 \text{ km s}^{-1}$ , respectively. This could indicate a line-of-sight component of the same motion seen as the narrowing of the gap. Alternatively, Kopp & Pneuman (1976) predict substantial outflow along field lines adjoining the current sheet. If those field lines are tilted

toward and away from Earth, Doppler shifts like those observed would naturally occur.

### 3. DISCUSSION AND CONCLUSIONS

Following Ciaravella et al. (2002), Ko et al. (2003), and Webb et al. (2003), the development of a current sheet in the wake of a CME is investigated once again. The event discussed here occurred on the east limb of the Sun on 2003 November 18. It started at 08:48 UT with the fast expansion of a group of sheared arcades. No apparent prominence structure can be recognized in either H $\alpha$  filtergrams or EIT 195 Å images prior to the eruption. This event developed a long and thin current sheet behind the CME. Magnetic reconnection inflow near the current sheet following the arcade expansion was observed, and the corresponding rate of magnetic reconnection  $M_A$  ranges from 0.01 to 0.23. The value of  $M_A$  in reality may not be constant and should cover a wider range.

A similar process of magnetic reconnection inflow was reported by Yokoyama et al. (2001) for the event on 1999 March 18. But the inflow velocity and  $M_A$  deduced by them are both 1 order of magnitude smaller than what we obtain in the present case. Another difference between the two events lies in the initial configurations. The magnetic arcades in the present case possess a much more compact structure than those of Yokoyama et al. (2001). The event observed by Yokoyama et al. started with the expansion of a feature that clearly manifests the “three-component” structure: a “bright leading edge,” a dark “void” or “cavity,” and a “bright core.” Here we are quoting the relevant terms because they are traditionally used for CMEs in progress (see Hundhausen et al. 1994; Low 2001), instead of for the structures prior to the eruption.

One of the advantages of this work over that of Yokoyama et al. (2001) is that the reconnection outflow in the present case might be observed. This allows us to estimate  $V_A$  directly in the reconnection inflow region in a more reliable way without making any extra assumptions. Furthermore, the UVCS observations make it possible for us to avoid unnecessary confusion in measuring the inflow speed of reconnection (see, e.g., Chen et al. 2004).

The morphological features of the CME developed by this event shown in Figure 5 nearly duplicate those of the diagram shown in Figure 1, which schematically describes the disrupted magnetic field that forms in the eruptive process following a catastrophic loss of equilibrium in the magnetic system. Comparing Figure 8 with Figure 5 further suggests that the typical Kopp-Pneuman structure is the low-corona component of a disrupting magnetic field. It is this disrupting magnetic field that provides both the major flare and the CME. Of course, the configuration in Figure 1 could also be produced in the processes described by other CME models, such as the sheared-arcade and breakout models (Mikić et al. 1988; Mikić & Linker 1994; Antiochos et al. 1999; Amari et al. 2003; Linker et al. 2003). Recently, Antiochos (2004) comprehensively compared the disrupted configuration produced by a catastrophe and that produced by breakout, concluding that they should have the same topological structure. The difference lies in the fact that the plasma inside the flux rope (CME core) in the former case should be cool (the prominence material) and that in the latter case is hot (the reconnected plasma flowing out of the current sheet). In the present case, the observations by UVCS just missed the CME core, and no information regarding the temperature of the plasma in the core can be drawn. Therefore, analyzing the available data for this event cannot help to determine which mechanism triggers the eruption.

The eruptive process manifested an energetic CME, with speeds of  $1939 \text{ km s}^{-1}$  at the front edge and  $1484 \text{ km s}^{-1}$  for the core, and a bright flare loop system covered by a cusp structure. This event was observed by various instruments from both space and the ground. Analyzing the observational data from these instruments yields the conclusion that the CME and the flare are connected by a stretched current sheet in which magnetic reconnection occurs and converts the magnetic energy into heat and kinetic energy. The morphological features of the disrupted magnetic field involved in this event fit those of the diagram shown in Figure 1 very well, which implies that this schematic depicts the common characteristics of the eruptive processes that give rise to both flare and CME. The magnetic

configuration in reality may be much more complex than that shown, but the fundamental physical processes should be the same.

J. L. is grateful to T. G. Forbes for valuable discussions. This work was supported by NASA under grants NNG04GE84G and NAG 5-12827 to the Smithsonian Astrophysical Observatory. The work of Y. J. and S. Z. was supported by the National Natural Science Foundation of China under grant 10173023 to the Yunnan Astronomical Observatory. *SOHO* is a joint mission of the European Space Agency and the US National Aeronautics and Space Administration.

## REFERENCES

- Amari, T., Luciani, J. F., Aly, J. J., Mikić, Z., & Linker, J. 2003, *ApJ*, 585, 1073
- Antiochos, S. K. 2004, Predictions of the Breakout Model for Interplanetary Observations (paper presented at the SHINE 2004 Workshop, Big Sky, MT)
- Antiochos, S. K., DeVore, C. R., & Klimchuk, J. A. 1999, *ApJ*, 510, 485
- Chen, P. F., Shibata, K., Brooks, D. H., & Isobe, H. 2004, *ApJ*, 602, L61
- Ciaravella, A., Raymond, J. C., Li, J., Reiaer, P., Gardner, L. D., Ko, Y.-K., & Fineschi, S. 2002, *ApJ*, 575, 1116
- Ciaravella, A., et al. 2000, *ApJ*, 529, 575
- Forbes, T. G. 2000, *J. Geophys. Res.*, 105, 23153
- Forbes, T. G., & Acton, L. W. 1996, *ApJ*, 459, 330
- Forbes, T. G., & Lin, J. 2000, *J. Atmos. Sol.-Terr. Phys.*, 62, 1499
- Forbes, T. G., & Malherbe, J. M. 1986, *ApJ*, 302, L67
- Gardner, L. D., Atkins, N., Fineschi, S., Smith, P. L., Kohl, J. L., Maccari, L., & Romoli, M. 2000, *Proc. SPIE*, 4139, 362
- Harrison, R. A., Bryans, P., Simnett, G. M., & Lyons, M. 2003, *A&A*, 400, 1071
- Hundhausen, A. J., Stanger, A. L., & Serbicki, S. A. 1994, in *Solar Dynamic Phenomena and Solar Wind Consequences*, ed. J. J. Hunt (ESA SP-373) (Noordwijk: ESA), 409
- Ko, Y.-K., Raymond, J. C., Lin, J., Lawrence, G., Li, J., & Fludra, A. 2003, *ApJ*, 594, 1068
- Kopp, R. A., & Pneuman, G. W. 1976, *Sol. Phys.*, 50, 85
- Lin, J. 2002, *Chinese J. Astron. Astrophys.*, 2, 539
- Lin, J., & Forbes, T. G. 2000, *J. Geophys. Res.*, 105, 2375
- Lin, J., Forbes, T. G., Priest, E. R., & Bungey, T. N. 1995, *Sol. Phys.*, 159, 275
- Lin, J., Raymond, J. C., & van Ballegoijen, A. A. 2004, *ApJ*, 602, 422
- Lin, J., Soon, W., & Baliunas, S. L. 2003, *NewA Rev.*, 47, 53
- Lin, R. P., et al. 2002, *Sol. Phys.*, 210, 3
- Linker, J. A., Mikić, Z., Lionello, R., Riley, P., Amari, T., & Odstrcil, D. 2003, *Phys. Plasmas*, 10, 1971
- Low, B. C. 2001, *J. Geophys. Res.*, 106, 25141
- Mikić, Z., Barnes, D. C., & Schnack, D. D. 1988, *ApJ*, 328, 830
- Mikić, Z., & Linker, J. A. 1994, *ApJ*, 430, 898
- Noci, G., Kohl, J. L., & Withbroe, G. L. 1987, *ApJ*, 315, 706
- Poletto, G., & Kopp, R. A. 1986, in *The Lower Atmosphere of Solar Flares*, ed. D. F. Neidig (Sunspot, NM: Natl. Sol. Obs.), 453
- Priest, E., & Forbes, T. 2000, *Magnetic Reconnection: MHD Theory and Applications* (Cambridge: Cambridge Univ. Press)
- Priest, E. R., & Forbes, T. G. 2002, *A&A Rev.*, 10, 313
- Qiu, J., Lee, J., Gary, D. E., & Wang, H. 2002, *ApJ*, 565, 1335
- Qiu, J., Wang, H., Cheng, C. Z., & Gary, D. E. 2004, *ApJ*, 604, 900
- Raymond, J. C., Ciaravella, A., Dobrzycka, D., Strachan, L., Ko, Y.-K., Uzzo, M. M., & Raouafi, A.-E. 2003, *ApJ*, 597, 1106
- Stenborg, G., & Cobelli, P. J. 2003, *A&A*, 398, 1185
- Starck, J.-L., Siebenmorgen, R., & Gredel, R. 1997, *ApJ*, 482, 1011
- Sui, L., & Holman, G. D. 2003, *ApJ*, 596, L251
- Sui, L., Holman, G. D., & Dennis, B. R. 2004, *ApJ*, 612, 546
- Švestka, Z. F., Fontenla, J. M., Machado, M. E., Martin, S. F., Neidig, D. F., & Poletto, G. 1987, *Sol. Phys.*, 108, 237
- Thompson, B. J., Cliver, E. W., Nitta, N., Delannée, C., & Delaboudinière, J.-P. 2000, *Geophys. Res. Lett.*, 27, 1431
- Wang, H., Qiu, J., Jing, J., & Zhang, H. 2003, *ApJ*, 593, 564
- Webb, D. F., Burkepile, J., Forbes, T. G., & Riley, P. 2003, *J. Geophys. Res.*, 108(A12), No. 1440
- Yokoyama, T., Akita, K., Morimoto, T., Inoue, K., & Newmark, J. 2001, *ApJ*, 546, L69